Geophys. J. Int. (2008) **173,** 142–156 doi: 10.1111/j.1365-246X.2008.03716.x

Effect of trench-outer rise bending-related faulting on seismic Poisson's ratio and mantle anisotropy: a case study offshore of Southern Central Chile

Eduardo Contreras-Reyes, Ingo Grevemeyer, Ernst R. Flueh, Martin Scherwath and Joerg Bialas

Leibniz-Institute of Marine Sciences (IFM-GEOMAR), Wischhofstr. 1–3, Kiel D-24148, Germany

Accepted 2007 December 20. Received 2007 November 16; in original form 2007 June 13

SUMMARY

Several trench-outer rise settings in subduction zones worldwide are characterized by a high degree of alteration, fracturing and hydration. These processes are induced by bending-related faulting in the upper part of the oceanic plate prior to its subduction. Mapping of *P*- and *S*-wave velocity structures in this complex tectonic setting provides crucial information for understanding the evolution of the incoming oceanic lithosphere, and serves as a baseline for comparison with seismic measurements elsewhere. Active source seismic investigations at the outer rise off Southern Central Chile (∼43°S) were carried out in order to study the seismic structure of the oceanic Nazca Plate. Seismic wide-angle data were used to derive 2-D velocity models of two seismic profiles located seaward of the trench axis on 14.5 Ma old crust; P01a approximately parallel to the direction of spreading and P03 approximately parallel to the spreading ridge and trench axes. We determined *P*- and *S*-velocity models using 2-D traveltime tomography. We found that the Poisson's ratio in the upper crust (layer 2) ranges between ∼0.33 at the top of the crust to ∼0.28 at the layer 2/3 interface, while in the lowermost crust and uppermost mantle it reaches values of ∼0.26 and ∼0.29, respectively. These features can be explained by an oceanic crust significantly weathered, altered and fractured. Relative high Poisson's ratios in the uppermost mantle may be likely related to partially hydrated mantle and hence serpentinization. Thus, the seismic structure of the oceanic lithosphere at the Southern Central Chile outer rise exhibits notable differences from the classic ophiolite seismic model ('normal' oceanic crust). These differences are primarily attributed to fracturing and hydration of the entire ocean crust, which are direct consequences of strong bending-related faulting at the outer rise. On the other hand, the comparison of the uppermost mantle *P*-wave velocities at the crossing point between the perpendicular profiles (∼90 km oceanward from the trench axis) reveals a low degree of P_n anisotropy (<2 per cent).

Key words: Seismic anisotropy; Seismic tomography; Subduction zone processes; Fractures and faults.

1 INTRODUCTION

Alteration and serpentinization of oceanic lithosphere entering the subduction zone has been postulated to arise from infiltration of sea water into normal faults in the trench-outer rise where oceanic plates bend upon entering subduction zones (e.g. Peacock 2001; Ranero *et al.* 2003). Here, the oceanic plate is largely altered by extensional stresses at the top of the lithosphere leading to normal faulting (Peacock 2001; Ranero *et al.* 2003), horst and graben structures (Ranero *et al.* 2003), and associated seismicity with tensional focal mechanisms (Chapple & Forrsyth 1979; Ranero *et al.* 2005). Additionally, bending-related faulting might open near vertical cracks and fissures, and reactivate pre-existing cracks previously created at the spreading centre. Hence, bending-related faulting modifies the porosity and permeability structure, and further provides the pathways for fluids to enter the crust and mantle (e.g. Ranero *et al.* 2003). This process has been evidenced by a notable reduction of compressional mantle velocities in the outer rise in several convergent margins. For example, reduced velocities of partially serpentinized mantle have been reported in subduction zones with little sediments such as North Chile (Ranero & Sallares 2004), Central Chile (Kopp *et al.* 2004) and Central America (Grevemeyer *et al.* 2007). In South Central Chile, the trench basin is heavily filled by terrigenous sediments sourced from the Southern Andes (Thornburg & Kulm 1987), and hydration of the oceanic listhosphere in the outer rise area is comparatively less vigorous (Contreras-Reyes

et al. 2007). Nevertheless, some regions of the outer rise are characterized by an oceanic basement exposed to the infiltration of sea water at high basement outcrops and extensional normal faults. Low compressional velocities and anomalous low heat flow values at the outer rise have been reported in this region, suggesting infiltration of sea water and perhaps hydro-alteration of the oceanic crust and upper mantle (Contreras-Reyes *et al.* 2007).

The Poisson's ratio (ν) is an indicator of lithology, porosity, structure and the existence of fluids within the rock. Theory predicts that for increasing fluid-content, V_s decreases faster than V_p resulting in the increase of ν (i.e. ν is more sensitive to the presence of fluids than P wave only). Therefore, mapping of ν would provides crucial evidence for existence of fluids within the oceanic lithosphere. Also, the presence of porosity, in the form of cracks and fissures, has a profound influence on seismic velocities and Poisson's ratios. High crack-porosity affects in disproportional amounts V_p and V_s, and it depends on the aspect ratios of the cracks (e.g. Shearer 1988; Takei 2002). Moreover, ν is quite sensitive to the grade of methamorphism (Christensen 1996), and it behaves differently depending on the mineral nature of the original rock. Differences between seismic Poisson's ratio measurements and laboratory analyses of ophiolites samples ('normal' oceanic crust) serve as an indicator to detect hydro-alteration and perturbation of the density structure of oceanic rocks. Theoretical prediction based on crack geometry and content of water have advanced in recent years (e.g. Takei 2002), but their application to geological settings rich in hydrothermal and faulting activity such as the outer rise areas has been limited by the difficulty of recording high-quality shear wave arrivals. During the TIPTEQ (from the Incoming Plate to Mega-thrust EarthQuake processes) experiment (Flueh & Grevemeyer 2005), *P* and *S* waves of high quality were recorded just 90 km oceanward from the Southern Central Chile trench (∼43°S). This data set allows us to image the uppermost ∼2 km of the mantle, and it provides an excellent opportunity to study the ν structure at the outer rise setting. Since fracturing and hydration process dramatically affects the Poisson's ratio structure of the oceanic crust and mantle, seismic *P*- and *S*-wave tomography should be able to detect this.

Another important issue related to the evolution of seismic properties at the outer rise is the study of upper mantle seismic anisotropy. Seismic anisotropy is initially controlled by the lattice preferred orientation (LPO) of relatively dry olivine at the creation of the oceanic lithosphere at mid-ocean ridges (Nicolas & Christensen 1987). Compressional waves travel fastest along the *a*-axis of relatively dry olivine, which generally matches the plate motion direction. However, several experimental and theoretical studies of P_n anisotropy have postulated that the presence of water affects considerably the preferential orientation of olivine. Olivine can be recrystallized and aligned along the *c*-axis nearly parallel to the shear direction when a large amount of water is present (Jung & Karato 2001). In our seismic experiment, we have recorded P_n phases of good quality along two mutually perpendicularly seismic profiles, yielding additionally the opportunity to investigate P_n anisotropy at the trench-outer rise off Southern Central Chile.

We modelled the velocity structure of the oceanic Nazca plate near the Southern Central Chile trench at ∼43°S along two perpendicular seismic wide-angle reflection and refraction transects. Seismic data recorded along one of these profiles allow us to identify refracted and reflected energy of shear waves, and they were used to construct a 2-D *S*-wave velocity model, and hence estimate Poisson's ratios. We used a joint refraction and reflection traveltime inversion approach to obtain accurate 2-D tomography velocity models (Korenaga *et al.* 2000), and *P*- and *S*-wave velocity model uncertainties are estimated by applying a non-linear Monte Carlo method (Korenaga *et al.* 2000). Finally, uppermost mantle velocities of the crossing profiles are compared to quantify P_n anisotropy at the outer rise, and it is interpreted within the tectonic framework.

2 TECTONIC SETTING

The geological structure of the Southern Central Chile margin is controlled by the subduction of the oceanic Nazca plate beneath South America. The incoming Nazca plate (approaching South America at a rate of ∼6.6 cm yr^{-1}) subducts at a relatively high convergence azimuth of ∼78°E (Angermann *et al.* 1999) (Fig. 1). The part of the plate investigated here has been formed at the Chile Rise (a fast spreading mid-ocean ridge). Fracture zones (FZs) cut the Chile Rise into several segments, resulting in abrupt changes of thermal states along the plate boundary. The Southern Central Chile trench is filled by terrigenous sediments sourced from the Andes (Thornburg & Kulm 1987), which are redistributed from south to north due to the slight northward dip of the trench floor (e.g. Thornburg *et al.* 1990).

Our study area corresponds to the outer rise located between Chiloe and Guafo FZs (Fig. 1). Here, the plate age decrease from 18.5 to 10 Ma along the Chile trench, and the half-spreading rate ranges between 45 and 35 mm a^{-1} (Tebbens *et al.* 1997). The plate age where the seismic profiles were positioned is approximately 12.5 Ma (Fig. 1). The spreading centre segments bounded by Chiloe and Guafo FZs are roughly parallel to the trench strike (Fig. 1). In the oceanward section of the outer rise, the plate is covered by a few hundred metres of pelagic sediments and turbidites (0–500 m) (Contreras-Reyes *et al.* 2007), whereas the sedimentary cover becomes thicker towards the trench owing to the turbiditic deposits filling the trench basin with a total thickness of ∼2 km at the trench axis (Scherwath *et al.* 2006). Active faulting underneath the sedimentary cover at the outer rise has been evidenced by several basement-faults imaged by highresolution seismic reflection data (Contreras-Reyes *et al.* 2007).

3 WIDE ANGLE SEISMIC DATA

Seismic measurements offshore South Central Chile were carried out using the German R/V SONNE during the TIPTEQ project (Flueh & Grevemeyer 2005). In this paper, we present the seismic wide-angle data that were collected along two seismic profiles (P01a and P03) located seaward of the trench axis, supplemented by high-resolution swath bathymetric images of the surrounding seafloor (Fig. 1). Seismic line P01a runs perpendicular to the Chile Rise spreading centre and approaches the deep sea trench roughly normal to the trench axis. Seismic line P03 runs parallel to the Chile trench and Chile Rise axes, and it crosses perpendicularly P01a (Fig. 1). Shots were recorded with a total number of 9 OBS (Ocean Bottom Seismometers) (Bialas and Flueh 1999) and OBH (Ocean Bottom Hydrophones) (Flueh & Bialas 1996). The seismic source for the refraction work was a cluster of 8 × 8-litres G-guns, providing a total volume of 64 litres for each shot. This source was fired at a time interval of 60 s, which corresponds to an average shot spacing of ∼150 m. The record sections were interpreted after bandpass filtering and predictive deconvolution. The signal-to-noise ratio obtained for most of the stations is high (Fig. 2). Crustal refractions (P_g), Moho wide-angle reflections (P_mP) and upper-mantle refractions (P_n) were recorded on almost all stations with excellent quality.

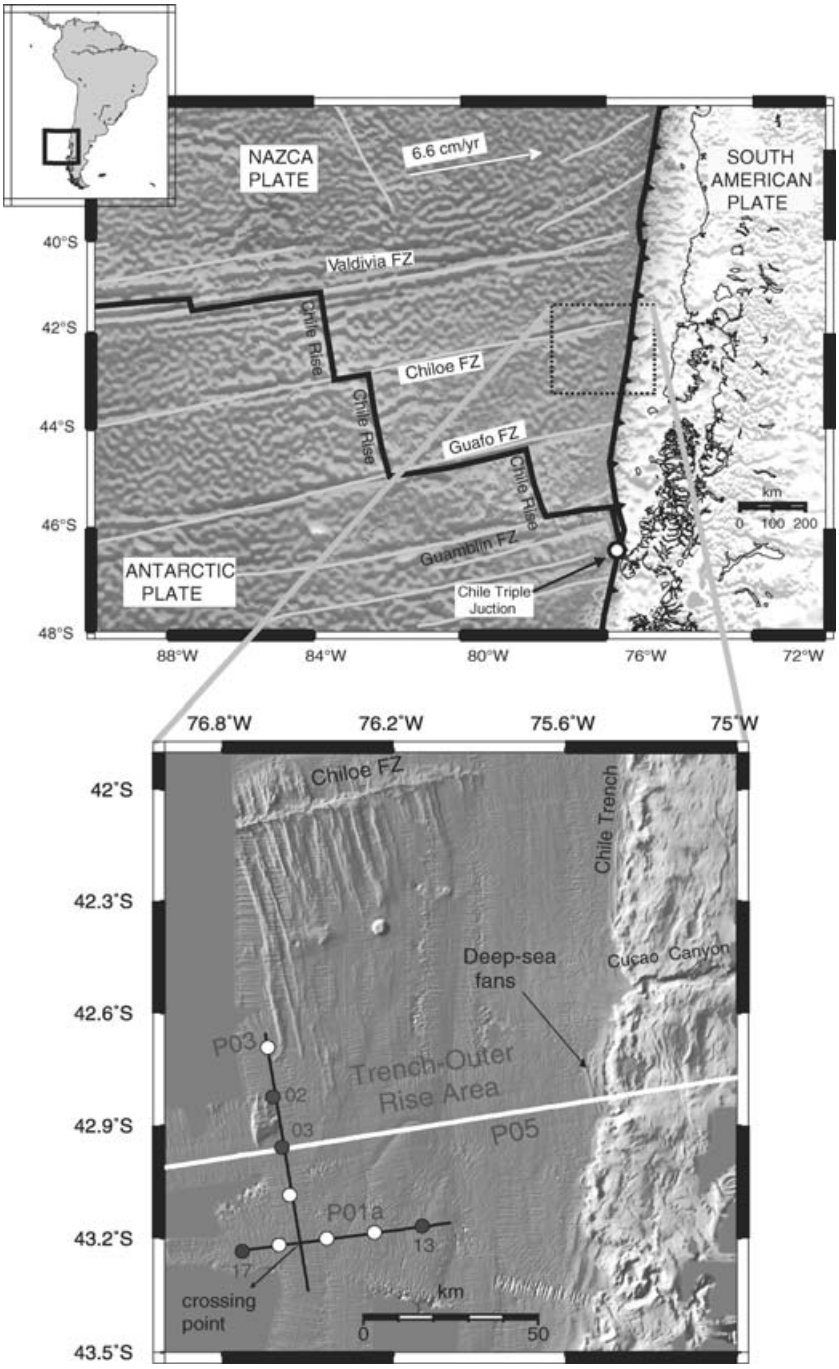

Figure 1. (top) Our study area is located between Chiloe and Guafo Fracture Zones, where the plate age ranges from 18.5 to 10 Ma along the Chile trench. (bottom) High-resolution bathymetric image of the incoming Southern Nazca plate, with locations of three wide-angle seismic profiles: P01a, P03 and P05. Black dots and station numbers indicate the four ocean bottom stations (17, 13, 02 and 03) shown in Fig. 2.

Four examples of seismic record sections are shown in Fig. 2, with their respective seismic phases identified.

The profile P01a, is a 65 km long east–west profile across the outer rise (Fig. 1), 85 km to the north of the Guafo FZ. This profile was recorded with 5 OBH/S evenly spaced every ∼8 km. All of them returned data with a high signal-to-noise ratio. The maximum shot receiver aperture was 62 km (Fig. 2a). Figs 2(a) and (b) show record sections representative of this profile with the identified P_g, P_mP and P_n phases. The 76 km long profile P03 is located ∼90 km west of the Chile trench (Fig. 1), which is covered by four OBSs spaced every ∼8 km. Figs 2(c) and (d) show record sections representative of this profile with the identified phases. P_mP and P_g phases are observed in most record sections with excellent quality. P_n arrivals are abundant in many stations (Figs 2c and d) with notable amplitude. The most striking feature of the dataset is the abundance of very strong *S*-wave arrivals, including Moho wide-angle reflections and *P*/*S* (*S*/*P*) conversions that can often be followed to offsets longer than 30 km. Shear-waves refractions S_g and S_n are observed in most record sections along P03, as well as *S*-wave Moho wide-angle reflections S_mS (Figs 2c and d).

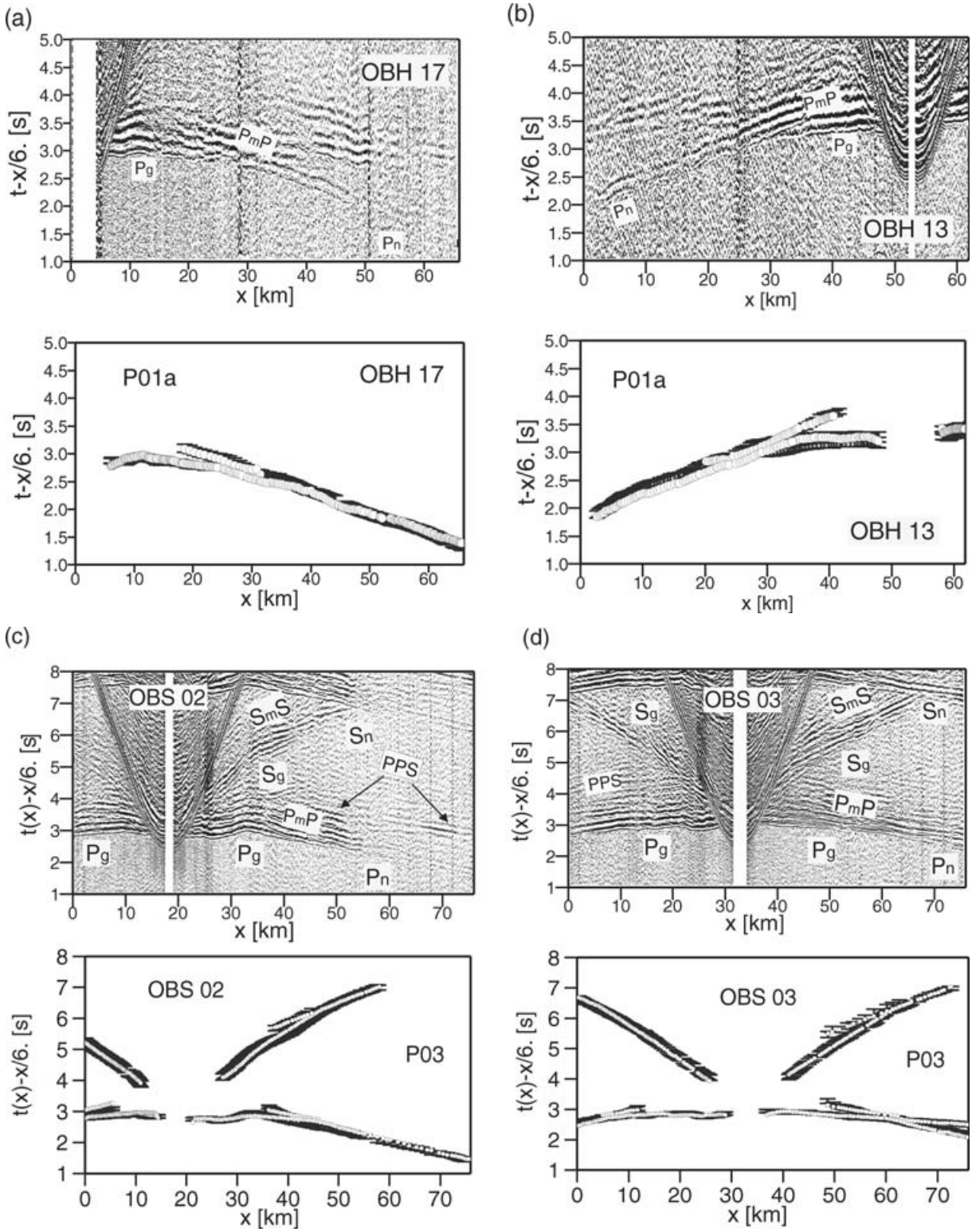

Figure 2. Examples of wide-angle seismic data with predicted traveltimes (white circles), which are computed based on the velocity model presented in Figs 3(a) and (b) and 4(a). (a) OBH 17, (b) OBH 13, (c) OBS 02 (hydrophone component) and (d) OBS 03 (hydrophone component).

Picking of the seismic phases was done manually, and picking errors were assigned on the basis of the dominant period of the phase. Detailed information regarding average picking uncertainties and number of picks for both profiles are summarized in Table 1. Typically, errors were assumed to be half a period of one arrival, to account for a possible systematic shift in the arrival identification, and were weighted according to the phase quality. Secondary S_g arrivals (arriving later than S_n) are not evident on the data. Moho reflections S_mS are identifiable on most of the stations (Figs 2c and d), although with relative high uncertainty (>80 ms).

Table 1. Summary of arrival time picks.

Phase	Profile	Total picks	ΔT_{avg} (ms
P_g	P01a	1335	55
P_mP	P01a	623	80
P_n	P01a	1052	70
Total[a]	P01a	3010	
P_g	P03	1541	55
P_mP	P03	438	75
P_n	P03	873	65
Total[a]	P03	2852	
$S_g + S_n$	P03	2294	80
S_mS	P03	336	100
Total[b]	P03	2630	

[a]Total number of picks for *P*-waves arrivals.
[b]Total number of picks for *S*-waves arrivals, and picking uncertainties (ΔT_{avg}) are given.

4 *P*-WAVE TRAVELTIME MODELLING SCHEME

We obtained the *P*-wave velocity–depth structure using the joint refraction and reflection traveltime inversion method of Korenaga *et al.* (2000). This method allows jointly inverting refraction (P_g and P_n) and reflection (P_mP) traveltimes for a 2-D velocity field. Traveltimes and ray paths are calculated employing a hybrid ray tracing scheme based on the graph method and the local ray bending refinement (van Avendonk *et al.* 1998). Smoothing constraints from predefined correlation lengths and optimized damping for the model parameters are employed to regularize an iterative linearized inversion (Korenaga *et al.* 2000).

The velocity models were constructed using four layers, (1) water, (2) sedimentary section, (3) oceanic crust and (4) upper mantle. To derive the velocity depth model, the water depths were taken from the known bathymetry, which remain fixed during the inversion. The basement was derived by a combined analysis of the reflection and refraction seismic data. Along P01a, we picked and converted the vertical incidence reflections from Two-way-Time (TWT) data (Flueh & Grevemeyer 2005) to depth using a constant velocity of 1.7 km s^{-1}. Along P03, no streamer data are available to establish the thickness of the sedimentary sequence. The basement depth was estimated from the seismic sections at each section, taking the multiples into account where the basement reflection is relative strong. Again, a constant velocity of 1.7 km s^{-1} was used for the sediments.

The sedimentary section was also held fixed in the inversion procedure. The *P*-wave velocity structure for the oceanic crust was inverted using P_g and P_mP phases in order to model the velocity field and Moho depth. Once the crustal structure was determined, this section remains fixed for the subsequent upper-mantle inversion, which is inverted using the P_n phases. Applying this hybrid technique not only the first arrivals are taken in account but also later refracted P_g could be used to constrain the lower crustal structure. To fix the structures obtained in the respective previous inversion, we defined 2-D velocity damping functions with either large or low weighting factors depending on the zone to retain or invert in the corresponding inversion (see Korenaga *et al.* 2000).

Horizontal grid spacing of the model used for velocity inversion is 0.5 km, whereas vertical grid spacing is varied from 0.05 km at the top of the model to 0.5 km at the bottom. Depth nodes defining the reflectors are spaced at 2 km. We used horizontal correlation lengths ranging from 2 km at the top to 10 km at the bottom of the model, and vertical correlation lengths varying from 0.4 km at the top to 2.5 km at the bottom. Several tests have shown that varying the correlations lengths by 50 per cent does not affect significantly the overall smoothness. In addition, there is a trade-off between correlation lengths and smoothing weights, and it is possible to obtain similar results with shorter correlation lengths and larger smoothing weights. Thus, we choose short correlation lengths and large smoothing weights in order to reduce memory requirements (Korenaga *et al.* 2000).

4.1. Oceanic crust tomography

We prepared a starting model for the crustal part by searching a 1-D velocity model that best fits the P_g and P_mP arrivals for each profile. The initial 1-D model, shown in the Appendix A, is composed of seismic layer 2 with a high vertical velocity gradient (>1.2 s^{-1}), and layer 3 with a low gradient (<0.2 s^{-1}). The starting Moho reflector was chosen as the sum of the obtained smoothed basement geometry and crustal thickness of 5.3 km, which was obtained previously from processing a longer wide-angle transect P05 (Contreras-Reyes *et al.* 2007) in the surrounding study area (see Fig. 1 for location). Initial and final root-mean-square traveltime misfits T_{rms} for the initial models are shown in Table 2. The starting models already yield a relative good fit, with a total (P_g and P_mP) $T_{rms} \sim 97$ ms and $T_{rms} \sim 92$ ms for profiles P01a and P03, respectively. This shows that the 1-D velocity model already fit the data well since the plate geometry is quite flat along these short profiles (particularly for profile P03 which runs parallel to the trench).

In order to study the accuracy of the final model, we apply the Monte Carlo method to estimate the uncertainties of the model (see Appendix for a description of this method). Figs 3(a) and (b) show the average model for both profiles obtained after application of the Monte Carlo method, with the inclusion of the upper mantle part of the model as explained below. T_{rms}, χ^2 parameters for the final average models are summarized in Table 2. The standard deviation of the calculated velocities σ_v for profile P01a and P03 are displayed in Figs 3(c) and (d), respectively. For the crustal part of the model along P01a, σ_v ranges between 0.05 and 0.2 km s^{-1}. Uncertainties of the Moho depth σ_z range between 0.1 and 0.3 km, average σ_z is less than 0.2 km. Maximum values of σ_v are reached at the eastern edge of the model (Fig. 3c) where the velocity uncertainty increases to values larger than 0.15 km s^{-1} and the maximum value of σ_z is $\sim$0.3 km.

Table 2. Details of seismic *P*-wave crustal velocity–depth inversion based on the average final models shown in Figs 3(a) and (b).

Phase	Profile	Initial T_{rms} (ms)	Initial χ^2	Average final T_{rms} (ms)	Average final χ^2
P_g	P01a	96.60	2.44	58.17	0.84
P_mP	P01a	97.26	1.93	79.37	1.28
Total ($P_g + P_mP$)	P01a	96.81	2.28	65.67	0.98
P_g	P03	90.22	2.20	56.87	0.86
P_mP	P03	96.65	2.49	81.86	1.72
Total ($P_g + P_mP$)	P03	91.64	2.26	62.4	1.05

T_{rms} = root-mean-square traveltime misfit,and χ^2 = chi-square parameter are given.

Table 3. Details of seismic *P*-wave mantle velocity inversion based on the average final models shown in Figs 3(a) and (b).

Phase	Profile	Average final T_{rms} (ms)	Average final χ^2
P_n	P01a	62.52	1.08
P_n	P03	60.58	1.04

T_{rms} = root-mean-square traveltime misfit, and χ^2 = chi-square parameter are given.

In this region the data coverage is reduced (Fig. 3c). Along profile P03, σ_v ranges between 0.05 and 0.2 km s^{-1} and $\sigma_z < 0.25$ km. Velocities uncertainties at the southern end of the upper crust reach values of 0.2 km s^{-1}, showing a reduced model resolution (Fig. 3d).

4.2. P_n traveltime tomography

For the subsequent tomographic inversion of the mantle refraction P_n, a 'layer-stripping' procedure was chosen, preserving the average velocity model and the average Moho interface gained before. Analogously, velocity uncertainties were estimated using the Monte Carlo approach (for details see Appendix). Initial and final T_{rms} for the initial and final models are shown in Table 3, respectively.

Along P01a, uncertainties of the upper-mantle velocity in the eastern part range between 0.05 and 0.15 km s^{-1} and are lower in the seaward part (<0.1 km s^{-1}) where the crustal velocity structure and Moho reflector are well constrained (Fig. 3c). In general, upper-mantle velocity uncertainties along P03 are less than 0.2 km s^{-1}, and become lower in the southern part ($\sigma_v \sim 0.1$ km s^{-1}) where there is good ray coverage of mantle phases.

A detailed comparison of P_n velocities of both profiles at the crossing point (Fig. 3) reveals that the difference between the velocities for these profiles is only 0.2 km s^{-1}, slightly more than the magnitude of the uncertainty in the velocity estimation. The faster P_n velocity is oriented in the direction of the spreading (along P01a). A similar estimation is obtained by comparing the uppermost-mantle velocity obtained along Profile P05 (Contreras-Reyes *et al.* 2007) with P03 at their intersection, which is located just 30 km to the north of the crossing point between P01a and P03 (see Fig. 1).

5 *S*-WAVE TRAVELTIME MODELLING SCHEME

Shear waves arrivals of good quality were recorded only along P03 (which is oriented parallel to the trench). Along P01a, in turn *S* waves are too weak to be included in our tomographic model. In general, conversion from *P*- to *S*-waves is more likely to occur where a sediment blanket is present (Lewis & McClain 1977), since cementation and infilling of cracks result in an increase of *S*-wave velocity and decrease shear attenuation enough for an efficient *P*- to *S*-wave conversion. The mature oceanic crust in our study area is covered by a sequence of 0–500 m of sediments, but the *P*- to *S*-wave conversion is preferentially efficient in the direction parallel to trench and inefficient perpendicular to it. Probably, the main reason is the

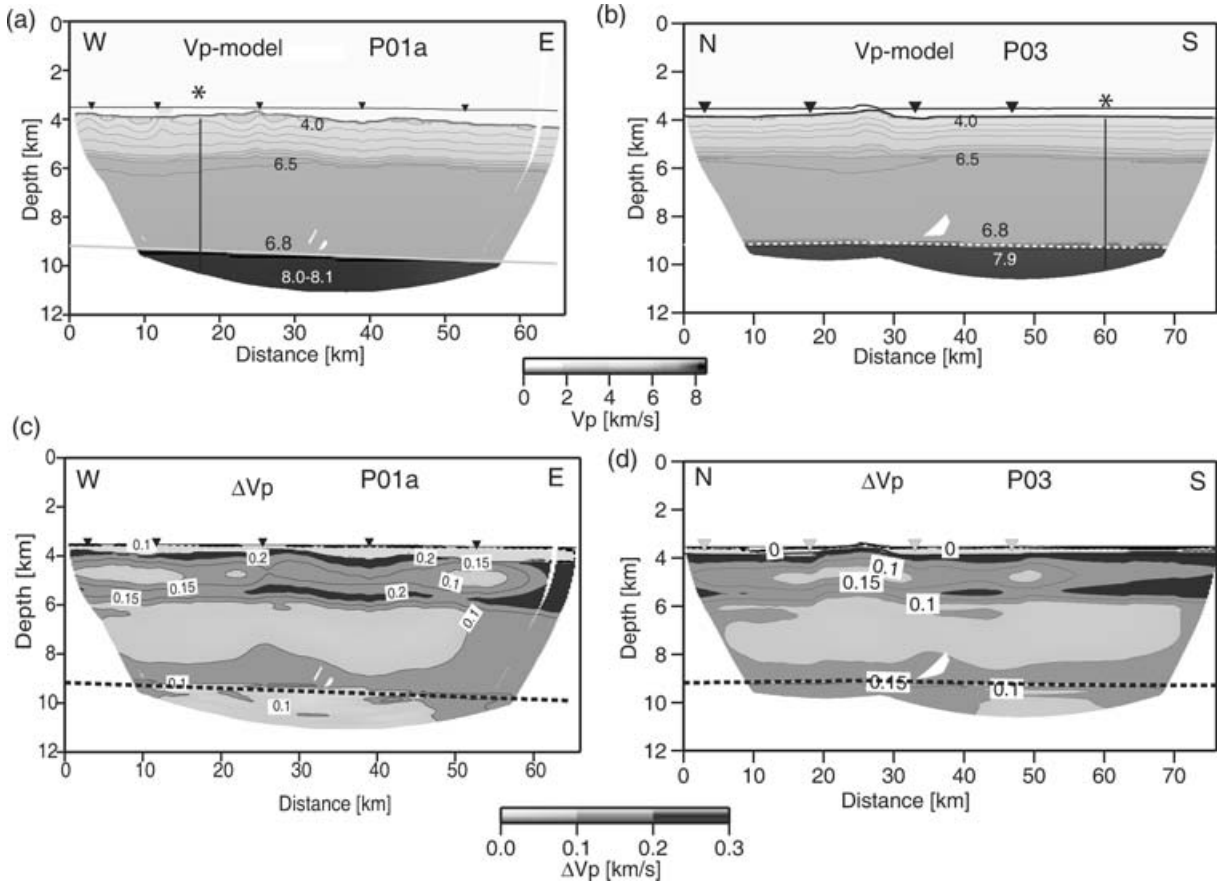

Figure 3. Result of *P*-wave velocity tomographic inversion. Final velocity model derived by averaging all Monte Carlo ensembles along (a) Profile P01a and (b) Profile P03. Asterisk in (a) and (b) denotes the location of the crossing point between P01a and P03. Corresponding standard deviation for compressional velocities along (c) P01a and (d) P03.

Table 4. Details of seismic shear wave arrivals inversion based on the average final models shown in Fig. 4(a).

Phase	$T_{\rm rms}$ (ms)	χ^2
$S_g + S_n$ (first arrivals)	72.70	0.95
$S_m S$	65.62	0.48
Total ($S_g + S_m S + S_n$)	71.88	0.89

$T_{\rm RMS}$ = root-mean-square traveltime misfit, and χ^2 = chi-square parameter are given.

topographic disturbances which parallel to the trench are small compared to the characteristic wavelength of the affected *S*-waves modes. Towards the trench, several extensional faults striking parallel to the trench axis (Fig. 7) result in a basement surface quite heterogeneous. Thus, the *P*- to *S*-wave conversion in the sediment-crust boundary near the trench is practically absent.

To obtain the shear velocity structure we assumed that the *P*- to *S*-wave conversion took place at the sediment/crust interface, and we fixed the layer interfaces of the *P*-wave velocity structure (sediment-crust, layer 2/3 and Moho boundaries) obtained previously (e.g. Mithal & Mutter 1989). Thus, only *S*-velocities values were altered in the tomographic inversion. Sedimentary velocities are not inverted in the seismic tomography, but they were estimated using the PPS wave modes. The PPS wave modes travel through the sedimentary layer and basement as a *P* wave and they are converted to an *S* wave at the sediment/crust interface, and hence is recorded as an *S* wave. Its time delay to the normal *P*-wave mode is directly related to the time difference in *P*- and *S*-wave velocity of the sediment section beneath the OBS station (e.g. Trummer 2002). We observed PPS phases on most of the stations, which exhibit the same apparent velocity as the first arrival *P*-phase but with a relative constant time delay of roughly 1 s (Figs 2c and d). Using the geometry and velocity field of the sedimentary section gained in the *P*-wave modelling, the estimated *S*-wave velocity is therefore $\sim$0.5 km s^{-1} in the sediments. The average picking uncertainty of PPS phases is 80 ms. Studying the traveltime error by perturbing *S*-wave velocities, we estimated an overall accuracy for shear wave velocities for the sedimentary layer of 0.05 km s^{-1}.

To model the oceanic crust and upper mantle simultaneously, we inverted only the first refracted shear wave arrivals (S_g and S_n) and Moho reflections $S_m S$. We used the PSP modes, where the signal travels as a *P* wave through the sedimentary layer but as an *S* wave through the oceanic crust (S_g and $S_m S$) and upper mantle (S_n). Picking uncertainties and number of picked arrivals of these phases are shown in Table 1. Starting model preparation and analysis of the uncertainties for the *S*-wave velocity model are described in the Appendix A. Figs 4(a) and (c) display the final average *S*-wave velocity model and its standard deviations, respectively. $T_{\rm rms}$ and χ^2 parameters are summarized in Table 4. Upper-crustal velocity uncertainties range between 0.05 and 0.25 km s^{-1}, with a mean value of $\sim$0.1 km s^{-1}. In general, $\sigma_{\rm v}$ through the lower crust is $<$0.15 km s^{-1}, its maximum where the poorest ray coverage is located at the southern edge. Velocity uncertainties in the upper mantle reach values of 0.1–0.2 km s^{-1}.

In Appendix B and C, we present two independent synthetic tests in order to study the robustness of our tomographic results. First, we study the traveltime sensitivity of the uppermost shear wave velocity by using classical 2-D forward modelling (Appendix B). Second, we modelled the most prominent amplitude pattern of the seismic data by using the method of reflectivity (Appendix C).

6 POISSON'S RATIO

The Poisson's ratio ν is the ratio of transverse contraction strain to longitudinal extension strain in the direction of stretching force. ν is related to the compressional wave velocity V_p and shear wave velocity V_s via

$$\nu = \frac{(V_p/V_s)^2 - 2}{2[(V_p/V_s)^2 - 1]} \tag{1}$$

and its standard error $\Delta\nu$ is given by:

$$\Delta\nu = \pm \frac{(V_p/V_s)^2}{[(V_p/V_s)^2 - 1]^2} \sqrt{\left(\frac{\Delta V_p}{V_p}\right)^2 + \left(\frac{\Delta V_s}{V_s}\right)^2}, \tag{2}$$

where ΔV_p and ΔV_s are the uncertainties of *P*- and *S*-wave velocities, respectively.

We used (1) to compute ν directly from the obtained *P*- and *S*-wave velocity structure at a common ray coverage, which is given by the overlap of the ray coverage of *P*- and *S*-wave velocity models (see Figs 3b, 4a and b). Uncertainties of the Poisson's ratio are computed using (2) and they are plotted in Fig. 4(d). Usually $\Delta V_p < \Delta V_s$, and thus $\Delta\nu$ is very sensible to the uncertainties of the *S*-wave velocity model. Characteristic values of $\Delta\nu$ range between 0.01 and 0.03, its maximum at the top of the oceanic crust (Fig. 4d).

7 RESULTS AND DISCUSSION

7.1 Seismic structure of the oceanic lithosphere

7.1.1 Sediments

The top of the incoming plate is covered by a mixture of pelagic and terrigenous sediments with compressional velocity of 1.7 km s^{-1} and shear wave velocity of 0.5 km s^{-1}, resulting in a Poisson's ratio of $\sim$0.48. The thickness of the sedimentary layer varies from 0 m (where igneous basement is exposed) to $\sim$500 m at the eastern most section of profile P01a (see Fig. 3a).

In situ measurements of shear wave velocity in marine sediments at less than 100 m below seafloor give ν values ranging from 0.46 to 0.49 (Hamilton 1976). Wilkens *et al.* (1992), based on inversion of *S*-wave velocities from full waveform acoustic logs recorded in partially lithified calcareous oozes, have determined Poisson's ratios of 0.35–0.39. We interpreted the Poisson's ratio of 0.48 for the sedimentary layer offshore of Southern Central Chile as a mixture-sequence of pelagic sediments and turbidites with rich water content.

7.1.2 Upper crust

Below the sediments, the velocity structure roughly follows the basement topography and a $\sim$1.7 km thick layer with compressional velocities between 4.0 $\pm$ 0.2 and 6.5 $\pm$ 0.15 km s^{-1} were obtained. Thus, seismic *P*-wave velocity is reduced by $\sim$0.5 km s^{-1} with respect to normal oceanic crust of that age (Grevemeyer & Weigel 1996; Grevemeyer *et al.* 1999). The shear-wave velocity at the top of the upper crust is 1.9 $\pm$ 0.2 km s^{-1}, hence the Poisson's ratio is 0.33 $\pm$ 0.03. *S*-wave velocity increases to 3.6 $\pm$ 0.15 km s^{-1} and $\nu = 0.27 \pm 0.02$ at the 2/3 layer boundary (Fig. 4b). The seismic structure is consistent with oceanic layer 2 with the typical sequence of extrusive basalts on top of a sheeted dikes complex (e.g. Vera *et al.* 1990). High V_p -gradient ($\sim$1.5 s^{-1}) and V_s-gradient ($\sim$0.9 s^{-1}) across seismic layer 2 is consistent with the rapid decrease of porosity, and consequently the decrease of ν with depth (Fig. 4b).

Lithology, degree of hydro-alteration, geometry and density of cracks influence the behaviour of ν. Discrepancies exist between

seismic Poisson's ratio measurements and laboratory analysis of ophiolites samples. For example, several *in situ* experiments have shown that the uppermost 200–300 m of the oceanic crust are consistent with Poisson's ratio of 0.32–0.38, which exceed values obtained for normal ocean basement samples ($\nu = 0.30$) (Salisbury & Christensen 1978; Hyndman 1979; Collier & Singh 1998). Spudich & Orcutt (1980) determined high values of ν (0.32–0.38) in the uppermost crust, which were interpreted as a high degree of porosity. High Poisson's ratios above 0.30 in the upper crust are typical for young oceanic crust due to its high porosity in the form of cracks, fissures, breccias and talus (e.g. Hyndmann 1979). Sediment thickening and filling of cracks by secondary minerals during crustal aging result in an increase of both *P*- and *S*-wave velocities (e.g. Wilkens *et al.* 1991), and a decrease of ν, as shown in laboratory studies (e.g. Shaw 1994). However, the relative mature oceanic crust (∼12.5 Ma) offshore South Central Chile is characterized by active faulting beneath the 'thick' sedimentary cover (Contreras-Reyes *et al.* 2007), reactivating fluid circulation and creating new cracks and re-opening old ones. Thus, additional pore space is created and hence porosity is increased at the outer rise owing to strong bending-related faulting. In this *in situ* experiment, we detected Poisson's ratios of ∼0.33 at the top of seismic layer 2, which are in close agreement with altered and fractured upper oceanic crust (Fig. 4b).

With increasing depth ν decreases to values of ∼0.28 at the base of the upper crust (Fig. 4b). Au & Clowes (1984) detected seismic Poisson's ratios of 0.22–0.26 at 1–1.5 km crustal depth, which are notably lower than for metamorphosed basalts (0.26–0.32) occurring at these depths in ophiolites. This difference between rock-laboratory and seismic measurements can be explained by crack theory. Shearer (1988) predicts that the Poisson's ratio is increased by the presence of thin cracks (aspect ratio <0.005) and is decreased by thick cracks (aspect ratio >0.5). At low depths both types of cracks are present, but thin cracks have a much greater effect on elastic properties than thick cracks (Shaw 1994). In contrast, Poisson's ratio is less sensible to porosity increment of thick cracks at shallow depths. At greater depth most of the thin cracks are closed and thick cracks dominate the behaviour of Poisson's ratio, resulting in its reduction. Shaw (1994) interpreted the depth pattern of cracks closures to be related to the aging of the ocean crust. In young crust thick cracks remain unsealed at depths of 1–1.5 km (Shearer 1988), and they gradually become sealed by hydro-mineral deposition as oceanic crust ages and sedimentary cover becomes thicker (e.g. Shaw 1994).

Our estimated Poisson's ratios of ∼0.28 at the base of layer 2 (∼1.7 km beneath sediments), fall between values of metamorphosed basalts (Fig. 6b). It is noteworthy that given the complexity and heterogeneity of crack-geometry perturbation caused by bending-related faulting, several scenarios might produce identical Poisson's ratio distribution, for example, fracturing and hydration acting simultaneously in the upper crust. On one hand, if active normal-faulting is able to increases the number of thick cracks, then according to the model of Shaw (1994) ν should decreases. On the other hand, if bending-related faulting allows the infilling of thick cracks by fluids, then ν should increase, contrasting the effect of thick cracks. Thus, hydro-fracturing effects may overprint

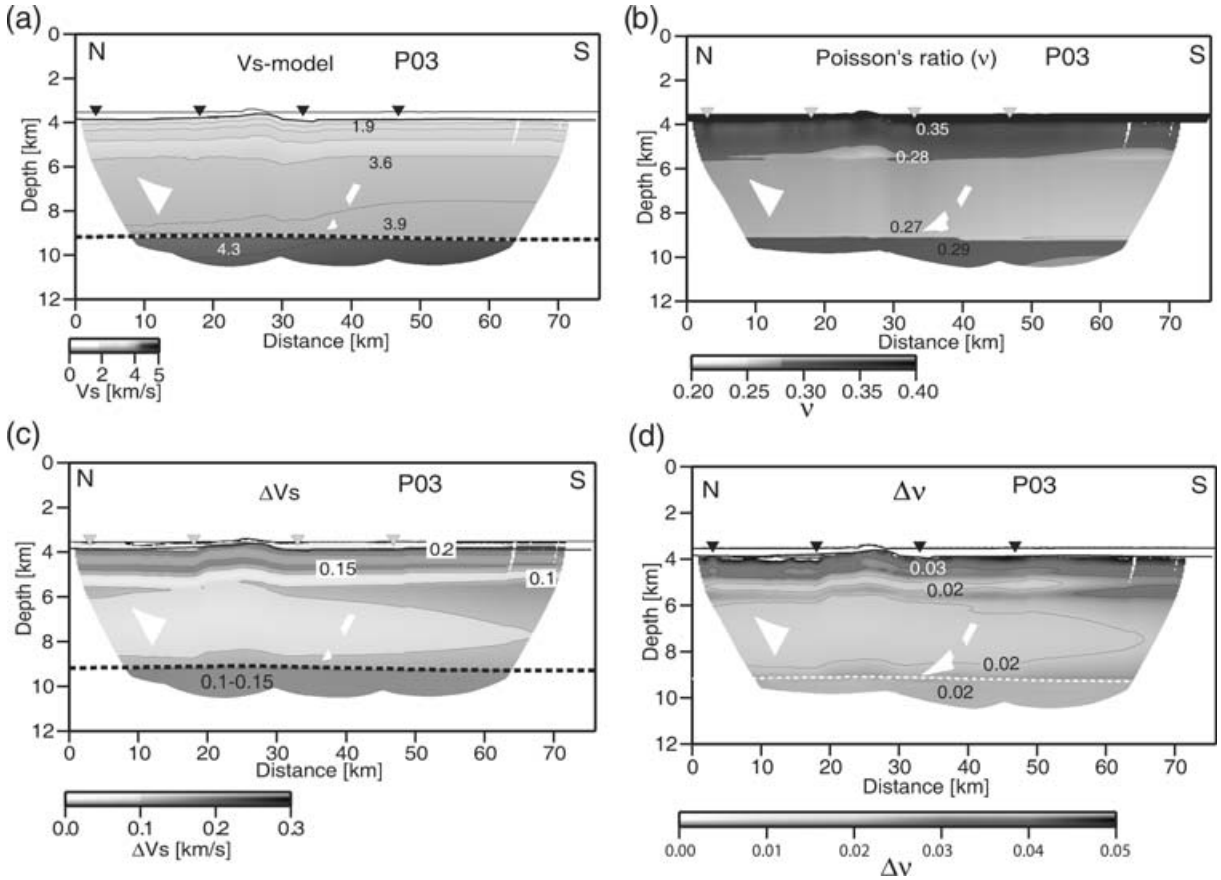

Figure 4. (a) Final shear wave velocity model derived by averaging all Monte Carlo ensembles. (b) Poisson's ratio two-dimensional model derived from V_p (Fig. 3b) and V_s (Fig. 4a) models at the same ray coverage intersection. (c) Standard deviation for *S*-wave velocity model. (d) Standard deviation for Poisson's ratio model.

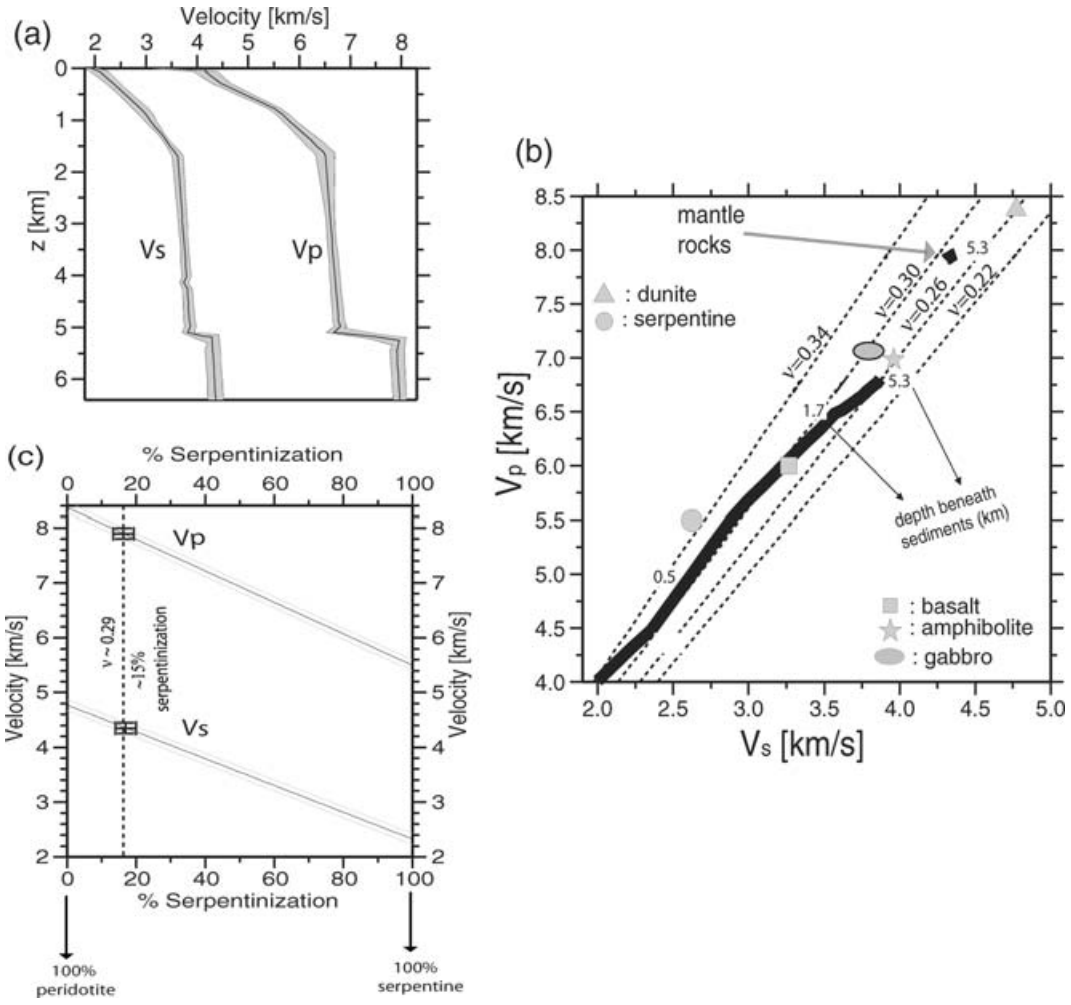

Figure 5. (a) Extracted compressional and shear velocity–depth profile at $x \sim 40$ km along profile P03. Grey area represents the velocity-uncertainty of the models. (b) *P* velocity versus *S* velocity paths for P03 (black solid line). Paths for constant Poisson's ratio (dot lines), which form straight lines in the V_p–V_s plane, are plotted at intervals of 0.04. V_p and V_s values for dunite, serpentinite, basalt, amphibolite and gabbro were taken at 200 MPa (Christensen 1996). (c) Trend of V_p and V_s as a function of degree of serpentinization based on compilation of laboratory mantle peridotite (Christensen 1996).

Poisson's ratio values of metamorphosed basalts. Since bending-related faulting modifies heterogeneously the bulk porosity, different distributions of distinct types of cracks should result in disproportional variations of the ν structure.

7.1.3 Lower crust

The upper crust overlies a ~3.6 km thick layer with compressional velocities increasing from 6.5 ± 0.1 km s^{-1} at the top of the layer to 6.8 ± 0.1 km s^{-1} at the bottom. Uppermost lower crust *S*-wave velocities are 3.6 ± 0.15 km s^{-1} and reach 3.8 ± 0.15 km s^{-1} at the Moho, resulting in a Poisson's ratio decreasing from 0.28 ± 0.02 to 0.26 ± 0.02 within the lower crust (Fig. 6b). The base of the lower crust is constrained by Moho reflections (P_mP) at about 5.3 km depth below the basement.

This seismic structure corresponds to oceanic layer 3, generally associated with gabbro and layered gabbro rocks (layer 3A and 3B). However, notable reduced lowermost crustal *P*-wave velocities (<7.0 km s^{-1}) suggest the likely presence of hydrous minerals such as chlorite and amphibolites (e.g. Hess 1962; Christensen & Salisbury 1975). Furthermore, Carlson & Miller (2004) pointed out that even in gabbros with top and bottom compressional velocities typical of seismic layer 3 (6.7 and 7.0 km s^{-1}, respectively) contain already 5–15 per cent alteration products, including 5–15 per cent amphibole and 0–5 per cent phyllosicates. Our estimates (6.5 and 6.8 km s^{-1}) are consistent with gabbros of high degree of metamorphism. Salisbury & Christensen (1978) determined ν values ranging from 0.26 to 0.31 based on experimental measurement of an ophiolite complex. Christensen (1996) reported ν values of 0.29 for gabbro decreasing with metamorphism to values as low as 0.26 for amphibolite facies rocks, based on measurements of V_p and V_s to hydrostatic pressures of 200 Mpa (Fig. 5, MPa).

Fracturing and population of cracks might also be partially responsible for the observed velocity reduction (e.g. Ranero & Sallares 2004). Old crustal cracks originally created at the spreading crest might be re-opened and new ones created by bending-related faulting near the trench, producing a large population of cracks at lower crustal depths. These cracks can be filled by infiltrated sea water via outer rise hydraulic faults, resulting in the hydro-alteration of the oceanic gabbro. Fig. 6(b) shows the reduction of ν within layer 3 between depths of 1.7 and 5.3 km beneath sediments, reaching a value of ~0.26 at the base of the crust. This value is clearly lower than laboratory measurements of gabbro rocks (~0.29) (Fig. 6b). According to the model of Shaw (1994), cracks of both small and

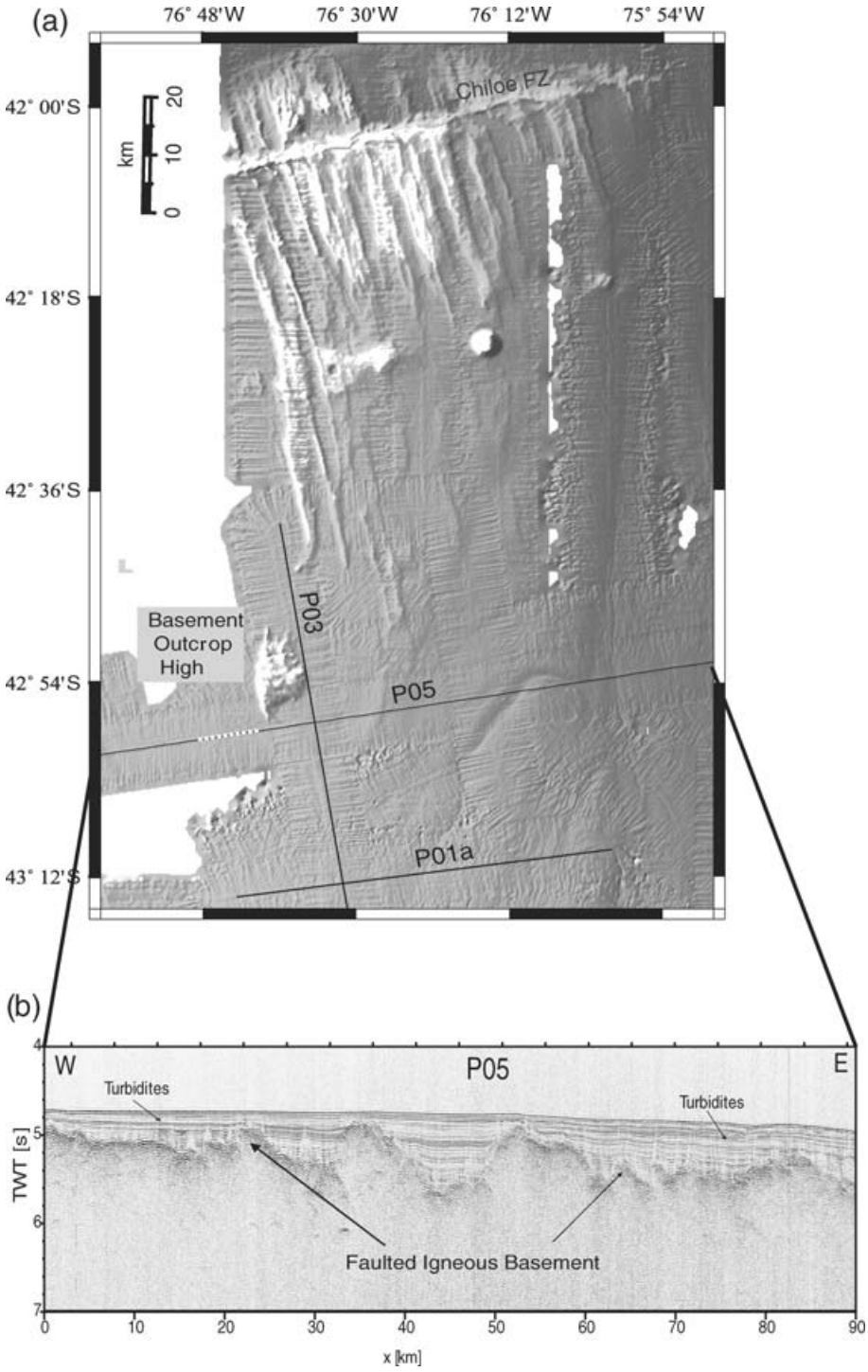

Figure 6. (a) High-resolution bathymetric image of the Southern Central Chile outer rise. (b) Multichannel reflection data reveals active faulting underneath the sedimentary cover, as it is shown by extensional bending faults, which cut the oceanic crust and expose igneous basement to direct contact with sea water.

large aspect ratios are closed at lower crustal depths, restoring Poisson's ratio values to be consistent with laboratory measurements (0.28–029). Our results near the Chile trench, however, show a decrease of ν rather than an increase within the lower crust (Fig. 6b). This implies that fracturing and/or hydro-alteration at lower crustal depths occurs, regardless that our seismic profile is emplaced on mature oceanic crust of ∼12.5 Ma, where usually hydrothermal alteration is largely confined to upper crustal depths (e.g. Carbotte & Scheirer 2004).

7.1.4 Uppermost mantle

Uppermost mantle V_p of 7.9 ± 0.1 km s^{-1} and V_s of 4.3 ± 0.15 km s^{-1} were detected along P03, which are lower than dry peridotite (V_p > 8.1 km s^{-1} and V_s > 4.6 km s^{-1}). Thus, along the Moho discontinuity a rapid increase of ν from 0.26 ± 0.02 at the lowermost crust to 0.29 ± 0.02 at the uppermost mantle is observed (Fig. 6b). Hyndman (1979) reported ratios of 0.24 (V_p/V_s = 1.71) with a compressional velocity of 8.4 km s^{-1} for mantle

peridotite. Based on laboratory samples of ophiolites, Christensen (1996) describes the transition from mafic to ultramafic igneous intrusions as a decrease of the Poisson's ratio reaching a value of ~0.26 ($V_p/V_s = 1.76$) immediately below the Moho. This ν reduction is due primarily to increasing dry olivine content. In the case of partially serpentinized mantle, however, the behaviour of ν is totally different, as Poisson's ratio increases abruptly where peridotite or dunite is hydrated. For example, serpentinization of dunite forces ν to change from an average 0.24–0.26 in peroditite to an average of 0.35 in serpentinite (Christensen 1996). Partially serpentinized dunites and peridotites have Poisson's ratios that fall between these limiting values.

Fig. 5c shows a compilation of V_p and V_s for mantle peroditite as a function of degree of serpentinization based on laboratory results of Christensen (1996). The data were taken at 200 MPa, and the average zero-serpentine for this suite of laboratory data is about 8.4 and 4.7 km s^{-1} for V_p and V_s, respectively. Our new tomographic results exhibit slightly reduced V_p and V_s, and high Poisson's ratios (~0.29) for mantle rocks reflecting a partial degree of hydration (Figs 5b and c). These values correspond to moderately hydrated mantle composition with a degree of serpentinization of 10–20 per cent (Fig. 5c). Since water is required to alter mantle peridotite to serpentinite, pervasive fracturing of the entire crust is suggested for the lithosphere entering the Chilean subduction zone off Chiloe Island.

7.2 Hydrothermal activity at the southern central Chile outer rise

The relative young oceanic Nazca plate created at the Chile Rise is characterized by the absence of a strong outer bulge oceanward from the trench axis and by a thick sedimentary cover. In some parts of the outer rise area shown in our bathymetric map, pelagic sediments and turbidites obscure normal outer rise faults (Fig. 6a). Since sediments are thought to limit sea water from communicating with the underlying oceanic crust, hydrothermal activity should be absent. However, seismic reflection data show some faults which expose basement, and also rough basement topography (Fig. 6b), suggesting that bending-related faulting pervasively fractures the oceanic crust beneath the sedimentary blanket and likely creates pathways for sea water into the uppermost brittle lithosphere. In addition, basement outcrops also expose igneous basement resulting in an easy percolation of cold sea water trough their flanks. Infiltration of cold sea water into the crust has been reported in the working area (Contreras-Reyes *et al.* 2007), where extremely low heat flow values in the outer-rise (~7 mW m^{-2}) are readily explained with the inflow of cold sea water trough a basement outcrop marked in Fig. 6(a). The seismic profile P03 passes next to the high basement outcrop and anomalous high Poisson's ratios in the oceanic crust in mantle are observed. Thus, hydration mechanisms in the oceanic plate provide a natural explanation for the velocity and Poisson's ratio anomaly.

7.3 P_n anisotropy at the outer rise

The genesis of the oceanic lithosphere involves active mantle flow, resulting in ductile deformation and intense crystal anisotropy of olivine within the uppermost mantle (Nicolas & Christensen 1987). Seismic anisotropy therefore is controlled by the lattice preferred orientation (LPO) of relatively water-poor olivine (Nicolas & Christensen 1987). *P* waves travel fastest along the *a* axis of relatively dry olivine. Hence, the direction of the fastest *P*-wave velocity is usually assumed to indicate the flow direction in the mantle (e.g. Zhang & Karato 1995). This assumption is not always valid, however, in environments with a large stress field and high water-content, such as subduction zones (Jung & Karato 2001). Experiments of Zhang & Karato (1995) show that at large strain, the main *a* axis orientation no longer follows the finite strain ellipsoid but rotates toward the shear direction. This process is also accompanied by intensive dynamic recrystallization. In addition, the presence of water can alter the relative strengths of olivine slip planes and change how it deforms (Jung & Karato 2001), and consequently results in variation of both degree and orientation of seismic anisotropy. Mineral physics studies showed that crystal anisotropy of wet peridotite is unusually low, despite of considerable texture strength (Precliz 2005). Furthermore, the hydration process enhances anisotropic deformation of olivine, increases with the amount of water and re-orients the fast wave speed orientation with the *c*-axis nearly parallel to the shear direction (Jung & Karato 2001).

Clowes & Au (1982), in an in-situ seismic experiment, reported strong P_n anisotropy of 10 per cent offshore western Canada (seaward from the trench), with a fastest speed of 8.3 km s^{-1} aligned parallel to the direction of the spreading and slowest of 7.5 km s^{-1} oriented approximately parallel to the spreading ridge. The difference was attributed to azimuthal velocity anisotropy of the type normally found in the Pacific basin. Christensen & Salisbury (1979) performed laboratory analyses of 15 ultramafic tectonite samples from an ophiolite complex, and they estimated a compressional seismic anisotropy of 6 per cent with a fastest upper-mantle velocity of 8.7 km s^{-1} parallel to the inferred spreading direction, and the slowest of 8.2 km s^{-1} perpendicular to this direction. Christensen & Smewing (1981) provide empirical results of harzburgites samples from the lower ultramafics of the Oman ophiolite. They found P_n anisotropy as high as 8 per cent. Our *in situ* P_n anisotropy estimation of ~2 per cent at the trench-outer rise area is considerably lower than the measurements mentioned above.

Fast P_n velocities of >8.3 km s^{-1} were detected >200 km seaward from the Southern Central Chile outer rise (Contreras-Reyes *et al.* 2007), reflecting a dry-peridotite composition of the oceanic mantle. However, towards the trench uppermost mantle velocities become systematically slower (~7.8 km s^{-1}) indicating an evolutionary process and alteration of the seismic properties of the oceanic lithosphere in the vicinity of the trench (Contreras-Reyes *et al.* 2007). We speculate, therefore, that tectonic and hydration processes near the trench decrease the difference between compressional velocities along the fast and slow axis of olivine or the partially serpentinized zones, and we anticipated that the fastest *P*-wave velocity orientation might be rotated while the plate approaches the trench, where hydrothermal circulation and stress magnitude increase. This interpretation is supported by laboratory experiments on mantle rocks (Zhang & Karato 1995; Jung & Karato 2001).

8 CONCLUSIONS

Joint inversion of seismic refraction and wide-angle reflection data at the Southern Central Chile outer rise yields the *P*- and *S*-wave velocity structure of the incoming oceanic Nazca Plate. We presented new results showing the impact of bending-related faulting on seismic properties of the oceanic subducting lithosphere prior to its subduction. This work leads to the following conclusions:

(i) The oceanic Nazca plate at the southern central Chile outer rise is covered by a sequence of oceanic pelagic sediments and

turbidites of 0–400 m, with a Poisson's ratio of ∼0.48. Frequently, the igneous basement with its extensional normal faults is exposed to direct contact with cold sea water.

(ii) The upper oceanic crust is characterized by relatively low V_p, low V_s, and high Poisson's ratios ranging between ∼0.33 at the top of the crust and ∼0.28 at the layer 2/3-interface. These high values of ν are interpreted to be the cause of high hydro-activity and high degree of porosity in the form of cracks and fissures.

(iii) The trend of Poisson's ratio within the lower crust is characterized by a slight decrease of ν from the top of the lower crust down to the Moho (where ν reaches values of ∼0.26 at the bottom of the crust). The observed decrease of ν is interpreted as the likely presence of a high degree of fracturing and/or hydro-alteration at lower crustal depths.

(iv) Anomalously high Poisson's ratios in the upper mantle of ∼0.29 are likely caused by partial hydration, since bending-related faulting may breach the entire oceanic crust providing the necessary water-pathways up to upper mantle depths. Based on laboratory seismic velocity measurements of mantle peridotite and serpentinite, the degree of serpentinization is 10–20 per cent.

(v) Comparison of the uppermost mantle velocities at the crossing points of perpendicular profiles reflects low degree of P_n anisotropy (<2 per cent). Our *in situ* refraction seismic experiment detected much lower degree of anisotropy than laboratory measurements of ophiolite complex and refractions experiments performed seaward from the outer rise area.

ACKNOWLEDGMENTS

We are grateful to Masters Kull and Mallon and their officers and crew of *RV Sonne* and all scientists who assisted in data collection during cruise SO181. Financial support was provided by the German GEOTECHNOLOGIEN programme jointly funded by the German Ministry of Education, Science, Research, and Technology (BMBF) and German Science Foundation (DFG), grants 03G0181A and 03G0594E. Eduardo Contreras-Reyes gratefully acknowledges a scholarship granted by the German Academic Exchange Service (DAAD). We would like to thank Emilio Vera and Arnim Berhorst for discussions on Amplitude modelling, as well as two anonymous reviewers for useful suggestions. This is GEOTECHNOLOGIEN publication no. GEOTECH-299.

REFERENCES

Angermann, D., Klotz, J. & Reigber, C., 1999. Space-geodetic estimation of the Nazca-South America Euler vector, *Earth planet. Sci. Lett.,* **171**(3), 329–334.

Au, D. & Clowes, R.M., 1984. Shear-wave velocity structure of the oceanic listhosphere from ocean bottom seismometers studies, *Geophys. J. R. astr. Soc.,* **77,** 105–123.

Bialas, J. & Flueh, E.R., 1999. Ocean bottom seismometers, *Sea Technol.,* **40**(4), 41–46.

Cande, S.C. & Leslie, R.B., 1986. Late Cenozoic tectonics of the southern Chile Trench, *J. geophys. Res.,* **91,** 471–496.

Carbotte & Scheirer, 2004. Variability of ocean crustal structure created along the global mid-ocean ridge, in *Hydrogeology of Oceanic Lithosphere,* pp. 128–150, eds Davis, E.E. & Elderfield, H., Cambridge University Press, New York.

Carlson, R.L. & Miller, D. Jay, 2004. Influence of pressure and mineralogy on seismic velocities in oceanic gabbros: implications for the composition and state of the lower oceanic crust, *J. geophys. Res.,* **109,** B09205, doi:10.1029/2003JB002699.

Chapman, C.H. & Orcutt, J.A., 1985. The computation of body wave synthetic seismograms in laterally homogeneous media, *Rev. Geophys.,* **23,** 105–163.

Chapple, W.M. & Forsyth, D.W., 1979. Earthquakes and bending plates at trenches. *J. geophys. Res.,* **84,** 6729–6749.

Christensen, N.I., 1996. Poisson's ratio and crustal seismology, *J. geophys. Res.,* **101**(B2), 3139–3156.

Christensen, N.I. & Salisbury, M.H., 1975. Structure and constitution of the lower oceanic crust, *Rev. Geophys.,* **13,** 57–86.

Christensen, N.I. & Salisbury, M.H., 1979. Seismic anisotropy in the oceanic upper mantle: evidence from the Bay of Islands ophiolite compley, *J. geophys. Res.,* **84,** 4601–4610.

Christensen, N.I. & Smewing, J.D., 1981. Geology and seismic structure of the northern section of the Oman ophiolite, *J. geophys. Res.,* **86,** 2545–2555.

Clowes, R.M. & Au, D., 1982. In-situ evidence for a low degree of S-wave anisotropy in the oceanic upper mantle, *Geophys. Res. Lett.,* **24,** 1311–1314.

Collier, J.S. & Singh, S.C., 1998. Poisson's ratio structure of young oceanic crust, *J. geophys. Res.,* **103**(B9), 20 981–20 996.

Contreras-Reyes, E., Grevemeyer, I., Flueh, E.R., Scherwath, M. & Heesemann, M., 2007. Alteration of oceanic subducting lithosphere at the southern central Chile trench-outer rise, *Geochem. Geophys. Geosyst.,* **8,** Q07003, doi:10.1029/2007GC001632.

Flueh, E.R. & Bialas, J., 1996. A digital, high data capacity ocean bottom recorder for seismic investigations, *Int. Underwater Syst. Design,* **18**(3), 18–20.

Flueh, E.R. & Grevemeyer, I., 2005. TIPTEQ SONNE Cruise SO-181 (Eds.), from the incoming plate to mega thrust earthquakes, *Geomar Rep. 102,* Geomar, Kiel, Germany.

Fuchs, K. & Mueller, G., 1971. Computation of synthetic seismograms with the reflectivity method and comparison with observations, *Geophys. J. R. astr. Soc.,* **23,** 417–433.

Grevemeyer, I. & Weigel, W., 1996. Seismic velocities of the uppermost igneous crust versus age, *Geophys. J. Int.,* **124,** 631–635.

Grevemeyer, I., Kaul, N., Villinger, H. & Weigel, W., 1999. Hydrothermal activity and the evolution of the seismic properties of upper oceanic crust, *J. geophys. Res.,* **104**(B3), 5069–5080.

Grevemeyer, I., Ranero, C.R., Flueh, E.R., Klaeschen, D. & Bialas, J., 2007. Passive and active seismological study of bending-related faulting and mantle serpentinization at the Middle America trench, *Earth planet. Sci. Lett.,* doi:10.1016/j.epsl.2007.04.013.

Hamilton, E.L., 1976. Shear-wave velocity versus depth in marine sediments: a review, *Geophysics,* **41**(5), 985–996.

Hess, H.H., 1962. History of ocean basins, in *Petrological Studies: A Volume in Honor of A. F. Buddington,* pp. 599–620, eds Engel, A.E., James, H.L. & Leonard, B.F., Geol. Soc. of Am., Boulder, Colo.

Hyndman, R.D., 1979. Poisson's ratio in the oceanic crust: a review, *Tectonophysics,* **59,** 321–333.

Jung, H. & Karato, S., 2001. Water-induced fabric transitions in Olivine, *Science,* **293,** 1460–1463.

Kopp, H., Flueh, E.R., Papenberg, C. & Klaeschen, D., 2004. Seismic investigations of the O'Higgins Seamount Group and Juan Fernández Ridge: aseismic ridge emplacement and lithosphere hydration, *Tectonics,* **23,** TC2009, doi:10.1029/2003TC001590.

Korenaga, J., Holbrook, W.S., Kent, G.M., Kelemen, P.B., Detrick, R.S., Larsen, H.-C., Hopper, J.R. & Dahl-Jensen, T., 2000. Crustal structure of the southeast Greenland margin from joint refraction and reflection seismic tomography, *J. geophys. Res.,* **105,** 21 591–21 614.

Lewis, B.T.R. & McClain, J., 1977. Converted shear waves as seen by ocean bottom seismometers and surface buoys, *Bull. seism. Soc. Am.,* **67,** 1291–1302.

Mithal R. & Mutter, J.C., 1989. A low-velocity zone within the layer 3 region of 118 Myr old oceanic crust in the western North Atlantic, *Geophys. J.,* **97,** 275–294.

Nicolas, A. & Christensen, N., 1987. *Composition, Structure and Dynamics of the Lithosphere-Asthenosphere System* eds Fuchs, K. & Froidevaux, C., pp. 111–123, Am. Geophys. Union, Washington, DC.

Peacock, S., 2001. Are the lower planes of double seismic zones caused by serpentine dyhydration in subducting oceanic mantle?, *Geology,* **29,** 299–302.

Precliz, R.M., 2005. Seismic anisotropy in peridotites from the Western Gneiss Region (Norway), laboratory measurements at high PT conditions and fabric based model predictions, *PhD thesis*, Swiss Federal Institute of Technology Zurich, Switzerland.

Ranero, C.R. & Sallares, V., 2004. Geophysical evidence for alteration of the crust and mantle of the Nazca Plate during bending at the north Chile trench, *Geology,* **32,** 549–552.

Ranero, C.R., Morgan, J. Phipps, McIntosh, K. & Reichert, C., 2003. Bending, faulting, and mantle serpentinization at the Middle America trench, *Nature,* **425,** 367–373.

Ranero, C.R., Villaseñor, A., Phipps, J. Morgan & Weinrebe, W., 2005. Relationship between bend-faulting at trenches and intermediate-depth seismicity, *Geochem. Geophys. Geosyst.,* **6,** Q12002, doi:10.1029/2005GC000997.

Salisbury, M.H. & Christensen, N.I., 1978. The seismic velocity structure of a traverse through the Bay of Islands ophiolite complex, Newfoundland: an exposure of oceanic crust and upper mantle, *J. geophys. Res.,* **83**(2), 805–817.

Scherwath, M., Flueh, E., Grevemeyer, I., Tilmann, F., Contreras-Reyes, E. & Weinrebe, W., 2006. Investigating subduction zone processes in Chile, *Eos Trans. AGU,* **87**(27), 265.

Shaw, P.R., 1994. Age variations of oceanic crust Poisson's ratio: inversion and a porosity evolution model, *J. geophys. Res.,* **99**(B2), 3057–3066.

Shearer, P.M., 1988. Synthetic seismogram modeling of shear-wave splitting in VSP data from the Geysers, California, *Geophys. Res. Lett.,* **15**(10), 1085–1088.

Spudich, P. & Orcutt, J.A., 1980. Petrology and Porosity of an oceanic crustal site: results from wave form modelling of seismic refraction data, *J. geophys. Res.,* **81**(5), 899–904.

Takei, Y., 2002. Effect of pore geometry on VP/VS: FROM equilibrium geometry to crack, *J. geophys. Res.,* **107**(B2), 2043, doi:10.1029/2001JB000522.

Tarantola, A., 1987. *Inverse Problem Theory: Methods for Data Fitting and Model Parameter Estimation,* 613 pp., Elsevier, New York.

Tebbens, S.F., Cande, S.C., Kovacs, L., Parra, J.C., LaBrecque, J.L. & Vergara, H., 1997. The Chile ridge: a tectonic framework, *J. geophys. Res.,* **102**(B6), 12 035–12 060, doi: 10.1029/96JB02581.

Thornburg, T.M. & Kulm, D.M., 1987. Sedimentation in the Chile Trench: depositional morphologies, lithofacies, and stratigraphy, *Geol. Soc. Am. Bull.,* **98,** 33–52.

Thornburg, T.M., Kulm, D.M. & Hussong, D.M., 1990. Submarine-fan development in the southern Chile trench: a dynamic interplay of tectonics and sedimentation, *Geol. Soc. Am. Bull.,* **102,** 1658–1680.

Trummer, I., 2002. S-wave processing and interpretation of wide-angle seismic refraction data, Malpelo ridge, eastern Panama basin, *PhD thesis*, Christian-Albrechts University, Kiel, 40–44 pp.

van Avendonk, H.J.A., Harding, A.J. & Orcutt, J.A., 1998. A two-dimensional tomographic study of the Clipperton transform fault, *J. geophys. Res.,* **103,** 17 885–17 899.

Vera, E.E., Mutter, J.C., Buhl, P., Orcutt, J.A., Harding, A.J., Kappus, M.E., Detrick, R.S. & Brocher, T.M., 1990. The structure of 0- to 0.2-m.y.-old oceanic crust at 9°N on the East Pacific Rise from expanded spread profiles, *J. geophys. Res.,* **95**(B10), 15 529–15 556, doi:10.1029/90JB00230.

Wilkens, R.H., Cheng, C.H. & Meredith, J.A., 1992. Evaluation and prediction of shear wave velocities in calcareous marine sediment and rocks, *J. geophys. Res.,* **97**(B6), 9297–9305.

Wilkens, R.H., Fryer, G.J. & Karsten, J., 1991. Evolution of porosity and seismic structure of upper oceanic crust: importance of aspect ratios, *J. geophys. Res.,* **96**(B11), 17 981–17 995.

Zhang, S. & Karato, S., 1995. Lattice preferred orientation of olivine deformed in simple shear, *Nature,* **375,** 774–777, doi:10.1038/375774a0.

APPENDIX

A. Monte Carlo test

In order to study the accuracy of the final model, we employed the Monte Carlo method (Korenaga *et al*. 2000). The uncertainty of a nonlinear inversion can be expressed in terms of the posterior model covariance matrix (e.g. Tarantola 1987), which can be approximated by the standard deviation of a large number of Monte Carlo realizations assuming that all the realizations have the same probability (e.g. Tarantola 1987). The uncertainty estimated by this method should be interpreted as the uncertainty for our model parameters (i.e. starting velocity model and smoothing constraints). The procedure to estimate velocity uncertainties consisted of randomly perturbing velocities of our reference model (Fig. A1). We generated 100 random initial velocity models by adding smooth perturbations randomly distributed (maximum velocity perturbations of ± 0.8 km s^{-1} at the top and ± 0.4 km s^{-1} at the bottom of the crustal reference models shown in Fig. A1). Maximum perturbations for the Moho reflector depth were ± 1.5 km. In addition to the perturbed reference models we produced 100 so-called noisy arrival time sets constructed by adding random phase errors (± 50 ms) and common receiver errors (± 50 ms) to the original data set (e.g. Korenaga *et al.* 2000). Then we performed a tomographic inversion for each velocity model with one noisy data set, in order to estimate not only the dependence of the solution on the reference model but also the effect of phase arrival time picking errors. The mean deviation of all realizations of such an ensemble is considered to be a statistical measure of the model parameter uncertainties (e.g. Tarantola 1987). All of the Monte Carlo inversions converged in less then seven iterations to $\chi^2 \sim 1$, where the model error is equal to the data uncertainty. In the upper mantle, we constructed several initial models by varying the uppermost-mantle velocity between 7.5 to 8.5 km s^{-1} and the mantle velocity gradient between 0 and 0.04 s^{-1}, respectively. The final average models and their uncertainties for profile P01a and P03 are plotted in Figs 3(c) and (d), respectively.

We prepare the V_s starting model by searching the best 1-D velocity model using a trial and error scheme. This velocity model is exhibited in Fig. A1 (black line). Similarly to the *P*-wave modelling, we perturbed this reference model and generated 100 initial models. Grey regions in Fig. A1 represent the possible variations of the velocity randomization. All of the Monte Carlo inversions converged in less then five iterations to $\chi^2 \sim 1$. Figs 4(a) and (c) show the average final *S*-wave velocity model and its standard deviations.

B. S_n traveltime sensitivity

We studied S_n velocity and different velocity gradients by keeping the shear velocity information above the Moho interface gained from previous crustal seismic tomography. Fig. B1 shows the record section of OBS 02, which displays an example of the onset of the S_n phase with an offset up to ~40 km. The best-fitting shear wave uppermost-mantle velocity is about 4.3 km s^{-1}, which is slow compared with dry peridotite (>4.7 km s^{-1}). A comparison with a higher S_n velocity of 4.6 km s^{-1} produces a S_n traveltime misfit of ~0.5 s, and so we conclude that the seismic data can only be explained by uppermost velocities as slow as 4.3 km s^{-1}.

C. Amplitude modelling

We calculated synthetic seismograms using the reflectivity method of Fuchs & Mueller (1971). Because the reflectivity method can

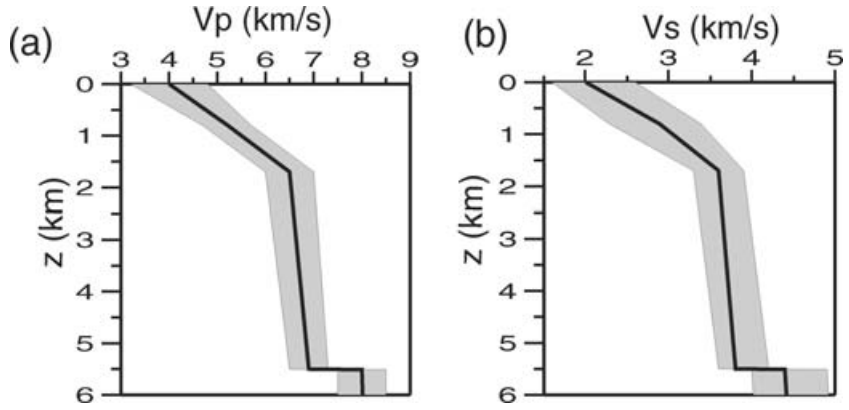

Figure A1. (a) Velocity reference models for the crustal part of the *P*-wave velocity models (black line). These models are based on the 1-D velocity models that best fits the P_g and P_mP arrivals for each profile. (b) Initial shear wave velocity model and range of velocities for Monte Carlo ensembles. For (1) and (2) velocity–depth profiles are shown beneath sediments, and grey areas represent the possible variations of the velocity randomization.

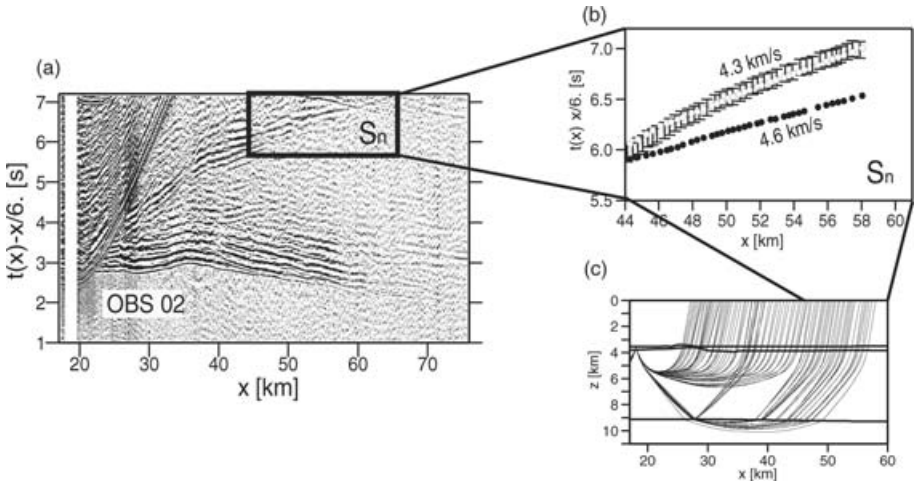

Figure B1. (a) Detailed forward analysis of S_n traveltimes for OBS 02. (b) S_n oceanic phases can only be predicted with values as slow as 4.3 km s^{-1} (white dots), typical uppermost *S*-wave velocities of 4.6 km s^{-1} produce a misfit >450 ms (black dots). (c) Corresponding ray paths.

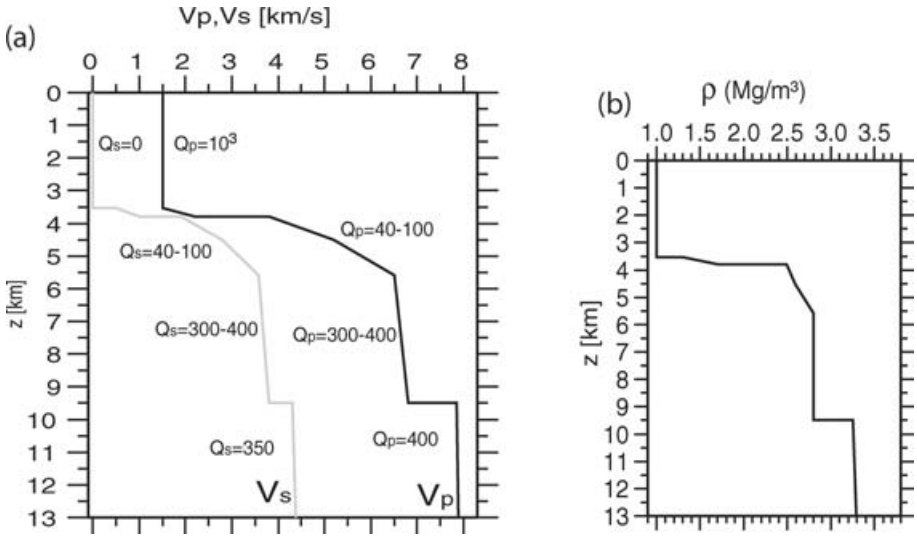

Figure C1. (a) 1-D *P*- and *S*-wave models determined from the amplitude analysis, and quality factors *Qp* and *Qs* are shown. (b) 1-D density model used during the computation of the synthetic seismograms.

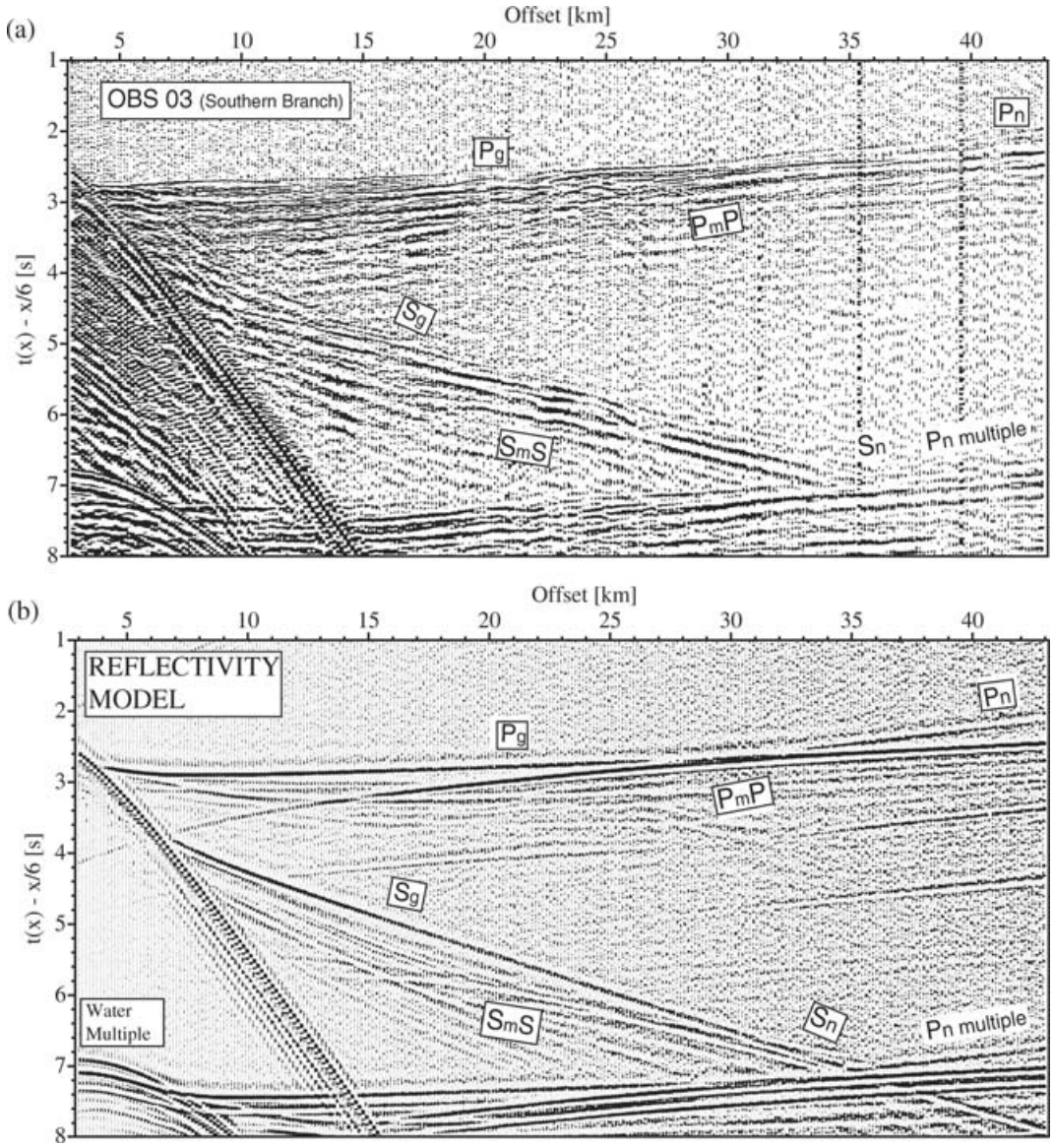

Figure C2. (a) Southern branch of record section OBS 03 (Hydrophone component) and main arrivals identified. (b) Synthetic seismograms at 150-m spacing computed using the reflectivity method based in our 1-D final model shown in Fig. C1.

deal only with constant-velocity layers, the velocity gradients were approximated using several uniform-velocity layers with a thickness of half the smallest wavelength present (Chapman & Orcutt 1985). We modelled the most prominent amplitude pattern of the southern branch of OBS 03 based on the final *P*- and *S*-wave velocity models derived by the tomographic inversion (Figs 3 and 4). We have chosen this branch of the station because it is less affected by the influence of the high topography of the basement outcrop (Fig. 1), which clearly produces 2-D effects on the traveltime pattern (see for example, Fig. 2). Nevertheless, two-dimensional effects linked to the variability of the basement topography and diffractions affect adversely the fit between the data and theoretical curves that are computed on a horizontal layer assumption. Fig. C1 exhibits the final 1-D velocity model obtained by using the reflectivity method, and quality factors (*Qp* and *Qs*), and density are shown. Fig. C2 shows the comparison of the data with the synthetic seismograms. In general, all major arrivals were reproduced by the synthetic models. A striking feature of the record section are the high-amplitudes of P_mP reflections at around 30 km offset, which marks the onset of the bright spot associated with the triplication point of the P_g, P_mP and P_n phases. This observation is nicely produced by the synthetic seismograms (Fig. C2). Moho *S*-wave reflections S_mS of notable amplitude between ∼17 and ∼35 km offset are also clearly produced by the reflectivity method, as well as all the main *P*-wave multiples (Fig. C2).